Molecular motor crossing the frontier of classical to quantum tunneling motion

Samuel Stolz[a,b], Oliver Gröning[a,1], Jan Prinz[a,b], Harald Brune[b], and Roland Widmer[a]

[a]Empa, Swiss Federal Laboratories for Materials Science and Technology, 8600 Dübendorf, Switzerland; and [b]Institute of Condensed Matter Physics, École Polytechnique Fédérale de Lausanne, 1015 Lausanne, Switzerland

The reliability by which molecular motor proteins convert undirected energy input into directed motion or transport has inspired the design of innumerable artificial molecular motors. We have realized and investigated an artificial molecular motor applying scanning tunneling microscopy (STM), which consists of a single acetylene (C_2H_2) rotor anchored to a chiral atomic cluster provided by a PdGa(111) surface that acts as a stator. By breaking spatial inversion symmetry, the stator defines the unique sense of rotation. While thermally activated motion is nondirected, inelastic electron tunneling triggers rotations, where the degree of directionality depends on the magnitude of the STM bias voltage. Below 17 K and 30-mV bias voltage, a constant rotation frequency is observed which bears the fundamental characteristics of quantum tunneling. The concomitantly high directionality, exceeding 97%, implicates the combination of quantum and nonequilibrium processes in this regime, being the hallmark of macroscopic quantum tunneling. The acetylene on PdGa(111) motor therefore pushes molecular machines to their extreme limits, not just in terms of size, but also regarding structural precision, degree of directionality, and cross-over from classical motion to quantum tunneling. This ultrasmall motor thus opens the possibility to investigate *in operando* effects and origins of energy dissipation during tunneling events, and, ultimately, energy harvesting at the atomic scales.

molecular motor | scanning tunneling microscopy | surface science

In 1959, Richard Feynman envisioned downscaling of information storage and machines to atomic dimensions (1). Both visions were eventually realized: by writing information via positioning single atoms on a nickel surface in 1990 (2), and by devising the first artificial, light-driven molecular machine in 1999 (3). The latter has been inspired by molecular machines in biological systems (4, 5) and led to the design of countless artificial molecular machines (6–12). However, most synthetic molecular machines, although driven by quantum processes, exhibit classical kinetics (13, 14), whereas operation by quantum tunneling motion is largely elusive. Scanning tunneling microscopy (STM) provides an ideal platform for investigating the dynamics of atoms and molecules on surfaces (10–12, 15–22). However, few studies were aimed at achieving controlled, STM-tip position-independent, directional motion that requires breaking of inversion symmetry, which is commonly achieved by adsorbing chiral molecules on achiral surfaces (10–12, 15). We reverse this concept by using the surface of noncentrosymmetric PdGa crystals as chiral stator. This relaxes the geometric constraints on the rotor molecule, and allows directed motion even for simple and symmetric molecules such as C_2H_2.

The starting point of our study is the creation of a well-defined chiral surface from a noncentrosymmetric single crystal, namely the intermetallic compound palladium–gallium with 1:1 stoichiometry (PdGa) exhibiting bulk-terminated chiral surfaces (23). The chiral structure of some of these surfaces manifests itself in pronounced enantioselective adsorption properties (24). Here we choose the threefold symmetric (111) surface of the PdGa A enantiomorph (23). Under appropriate ultrahigh vacuum preparation, it terminates by a layer containing three Pd atoms per

trigonal surface unit cell ($a_0 = 6.95 Å$) forming an equilateral triangle of 3.01 Å side length (*SI Appendix*, Fig. S1 and ref. 25). The local inversion symmetry of this Pd trimer is lifted by coordination of the six second-layer Ga atoms and furthermore by three Pd atoms in the third layer (Fig. 1 *A* and *B*). In the following we will denote this termination as Pd_3.

On Pd_3, acetylene molecules adsorb on top of the Pd trimers (26). When imaged by STM at 5 K, they appear as dumbbells with lobe-to-lobe separation of about 3 Å in three symmetrically equivalent 120°-rotated orientations (Fig. 1 *E–G*) between which they switch quasiinstantaneously (Fig. 1 *C* and *D*). Acetylene molecules are firmly anchored to the trimer and usually dissociate before being dragged off the trimer by STM-tip manipulation.

We have followed the rotation events by recording tunneling current time series $I_T(t)$ at a fixed tip position (Fig. 1H), in analogy to the STM investigation of the rotation of chiral butyl–methyl–sulphide on Cu(111) (10). In the latter case, a weak ($\leq 5\%$) asymmetry in the number of clockwise (CW) n_{CW} and counterclockwise (CCW) n_{CCW} rotations was reported and tentatively attributed to chiral STM tips, as no correlation of the directionality with the molecule's enantiomeric form was found. The $I_T(t)$ of Fig. 1H, recorded over $\Delta t = 100$ s, exhibits cyclic jump sequences between three levels ($\ldots R_A \rightarrow R_B \rightarrow B_C \rightarrow R_A \ldots$) with $n_{CCW} = 23$ jumps in the CCW direction and $n_{CW} = 0$ in CW, resulting in a frequency $f = \frac{n_{CCW} + n_{CW}}{\Delta t} = 0.23$ Hz and perfect directionality $dir = 100\% * \frac{n_{CCW} - n_{CW}}{n_{CCW} + n_{CW}} = 100\%$. Movie SV1 shows a

Significance

Conversion of undirected energy input into directed motion on molecular scales is the basis for controlled movements in living organisms. In this context, fundamental insights can be obtained by investigating artificial molecular machines under well-defined conditions. We devised the currently smallest, atomically precise molecular machine, whose rotor (C_2H_2) consists of just four atoms and whose functioning we have tracked employing scanning tunneling microscopy (STM). Unlike all other reported surface-anchored rotors, ours is characterized by an extremely high degree of directionality which is independent of STM-tip condition or position, therefore solely defined by the chiral support. Owing to its ultrasmall size, our rotor's operation crosses the well-established classical to an unanticipated quantum tunneling kinetic regime without loss in directionality.
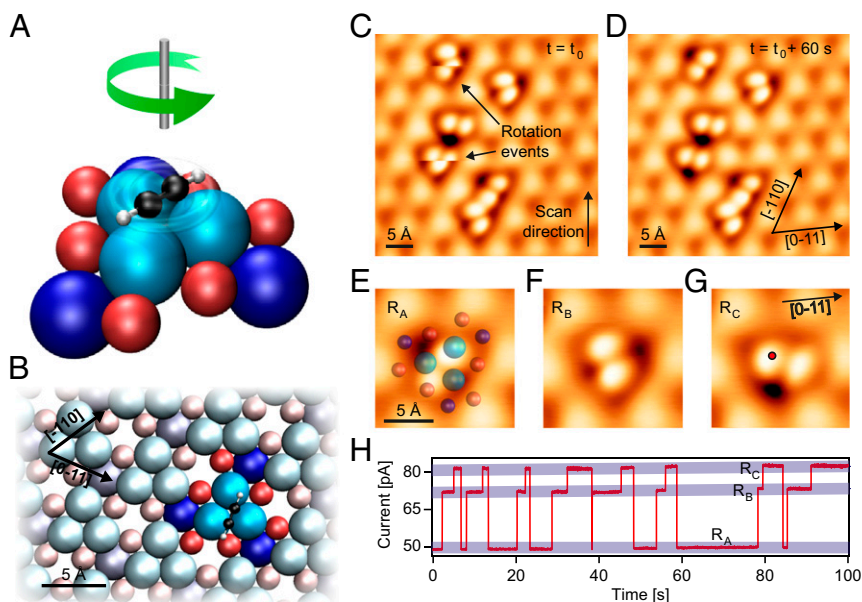
Fig. 1. Acetylene rotation on the PdGa:A($\overline{1}\overline{1}\overline{1}$)Pd$_3$ surface. (*A*) Sketch of the acetylene (C$_2$H$_2$) on Pd$_3$ motor. (*B*) Atomic structure of the PdGa:A($\overline{1}\overline{1}\overline{1}$)Pd$_3$ surfaces with the PdGa cluster acting as stator highlighted in saturated colors. The C$_2$H$_2$ rotor is depicted in one (R$_a$) of its three equivalent adsorption configurations R$_a$, R$_b$, R$_c$. In *A* and *B*, the top-layered Pd trimers ($z = 0$) are depicted in bright blue, the second-layer Ga trimers ($z = -0.85$ Å) in red, and the third-layered single Pd atoms ($z = -1.61$ Å) in dark blue. (*C–G*) Constant current STM images of C$_2$H$_2$ adsorbed on the Pd$_3$ surface ($T = 5$ K; $V_G = 10$ mV; $I_T = 50$ pA). In *C* two rotating molecules are pointed out, whereas in *D*, recorded 60 s after *C*, no molecular rotation is observed. (*E–G*) STM images of the same acetylene molecule in its three rotational configurations. In *E* the underlying PdGa stator structure is superposed. (*H*) Tunneling current time series $I_T(t)$ ($\Delta t = 100$ s; $V_G = 25$ mV; 1-ms time resolution) measured at the relative position to the C$_2$H$_2$ indicated by the red marker in *G*.

time-lapse series of STM images evidencing the prevailing CCW rotation of the motor.

Analyzing the parametric dependence of the rotation frequency (Fig. 2 *A–C* and *SI Appendix*, Fig. S2) shows that this molecular motor operates in two distinct regimes; the tunneling regime (TR) where its rotation frequency ν_T is independent of temperature $T < 15$ K, bias voltage $|V_G| < 30$ mV, and current $I_T < 200$ pA, and the classical regime (CR) where the frequency

strongly depends on these parameters. Even though all experimental data presented in Fig. 1 have been recorded in the TR, we first discuss the CR where C$_2$H$_2$ rotations can be selectively powered by thermal or electrical excitations. We find the temperature dependence of the rotation frequency at low bias (Fig. 2*A*) to follow an Arrhenius characteristic (solid line in Fig. 2*A*) $\nu(T) = \nu_T + \nu_A \exp\left(-\frac{\Delta E_B}{k_B T}\right)$ **[1]**, with $\nu_T = 4.5$ Hz, $\nu_A = 10^{8.7 \pm 2.0}$ Hz (attempt frequency), and $\Delta E_B = 27.5 \pm 7.1$ meV
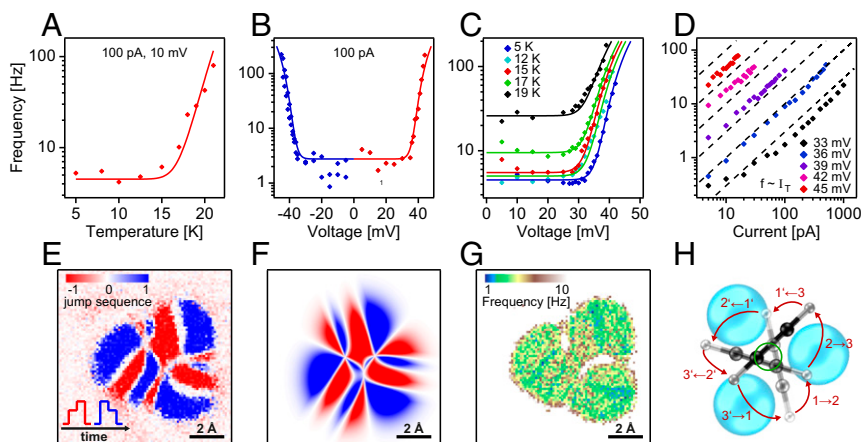
Fig. 2. Parametric dependence of the rotation frequency and jump sequence. (*A*) Rotation frequency dependence on temperature ($V_G = 10$ mV; $I_T = 100$ pA), *B* on bias voltage for both polarities ($T = 5$ K; $I_T = 100$ pA), *C* on bias voltage at various temperatures between 5 and 19 K; $I_T = 100$ pA), and *D* on tunneling current for different bias voltages between 33 and 45 mV at $T = 5$ K. In *A–D*, the markers represent experimental data, while the solid lines are derived from the kinetic model (*SI Appendix*). (*E*) Constant current jump-sequence map ($js = 3*\frac{n_{up}-n_{down}}{n_{up}+n_{down}} = sign(js)*|dir|$; $n_{up/down}$: number of jumps increasing/decreasing the tip height) generated from an 80×80 grid (1×1 nm^2) of individual tip-height time series $z_T(t)$, each recorded for 4 s (4,000 points; $V_G = 10$ mV; $I_T = 100$ pA). (*F*) Simulated jump-sequence map for a 100% CCW rotation based on the motion pattern shown in *H*. (*G*) Frequency map of the C$_2$H$_2$ rotation extracted from the same experimental $z_T(t)$ grid of *E*. (*H*) Our best estimation of the tumbling acetylene rotation on Pd$_3$ for a full 360° rotation in six 60° steps indicated by tracking the motion of one H atom ($1\rightarrow2\rightarrow3\rightarrow1'\rightarrow2'\rightarrow3'$ with n and n' denoting indistinguishable C$_2$H$_2$ configurations) with the green circle indicating the motion of acetylene's center of mass.

(energy barrier for rotation). Above 30 mV the frequency increases exponentially with V_G, independent of polarity (Fig. 2 *B* and *C*). Under the same conditions, but at constant bias voltage, the power-law dependence $\nu \propto I_T^n$ with $n \approx 1$ (Fig. 2*D*) identifies the electronically stimulated rotation as a single-electron process (27). As we will discuss later, the parametric dependence of the rotation frequency and directionality with T, V_G, and I_T is very well reproduced by a Langevin kinetic model (solid lines in Fig. 2 *B* and *C*).

Before we discuss the parametric dependence of the directionality, the influence of the STM tip, required for observing the motion, must be clarified. Particularly, we have to verify that breaking of the inversion symmetry due to the tip position (and possibly tip structure) in proximity to the motor does not prevail over the influence of the chiral substrate in determining the sense of rotation. To address this issue, we have measured 6,400 constant current tip-height time series $z_T(t)$ on a grid of 80×80 equidistant points covering $1 \times 1 \text{ nm}^2$ in the vicinity of single acetylene molecules in the TR. Analysis of all these $z_T(t)$ series reveals an intricate, regular pattern with alternating, highly directional ascending (red) and descending (blue) jump sequences (Fig. 2*E*). This pattern fully corroborates a tip-position-independent, unidirectional rotation of the molecule, which becomes apparent by modeling and mapping the position-dependent jump sequence assuming a cyclic unidirectional CCW rotation of the molecule by 60° steps (*SI Appendix*, Figs. S4–S7). After optimizing molecule configuration and tip shape in the model, an excellent agreement of the simulated jump-sequence map (Fig. 2*F*) with the experiment is found. Hence, we conclude that, regardless of the tip position, the jump sequences always correspond to CCW rotations. Furthermore, as witnessed from Fig. 2*G*, there is no pronounced dependence of ν_T on the tip position, and all three rotational C_2H_2 configurations can be expected to be energetically equivalent, as derived from the residence time analysis in *SI Appendix*, Figs. S8–S10. The three rotational states only become energetically nondegenerate if the tip is brought very close to the substrate, such that it significantly alters the surface ratchet potential (*SI Appendix*, Fig. S3). Although we investigated hundreds of molecules with tens of different tip modifications, we never observed any systematic CW rotations in the TR or CR evidencing that solely the stator dictates the direction and directionality of the rotation. Evaluating 1,792 rotation events ($n_{CCW} = 1,771$ and $n_{CW} = 21$) in the TR, we determine a directionality $dir \geq 96.7\%$ with 2σ confidence. By matching the simulated jump-sequence map to the experiment we identify the C_2H_2 rotation to be best described as a tumbling rotor, whose center of mass moves on a circle with radius $r = 0.5 \pm 0.1$ Å and a moment of inertia $I_{C_2H_2} = 5.62 \times 10^{-46} \text{kgm}^2$ (Fig. 2*H*).

Having clarified the influence of the tip, we now turn to the discussion of the parametric dependencies of the directionality (Fig. 3 *A–D*). The temperature dependence shows a rapid drop in directionality once thermally activated rotations start to contribute significantly. The solid line in Fig. 3*A* assumes that ν_T exhibits 98% directionality, whereas the thermally activated jumps described by the Arrhenius equation **1** are purely random. These random thermal rotation events are expected because substrate, STM tip, and hence molecule are in thermal equilibrium and, accordingly, unidirectional rotation (which reduces entropy) is forbidden by the second law of thermodynamics. At $T = 5$ K a decrease of directionality is also observed for bias voltages V_G beyond ± 35 meV (Fig. 3*B*). However, unlike thermal rotations, those induced by inelastic electron tunneling (IET) only become gradually nondirectional. This is clearly observed in the regime where thermally and IET induced rotations coexist. As displayed in Fig. 3*C*, the voltage-independent directionality of only 10% at $T = 19$ K and $|V_G| < 30$ mV, can be increased significantly at higher $|V_G|$ due to additional directed
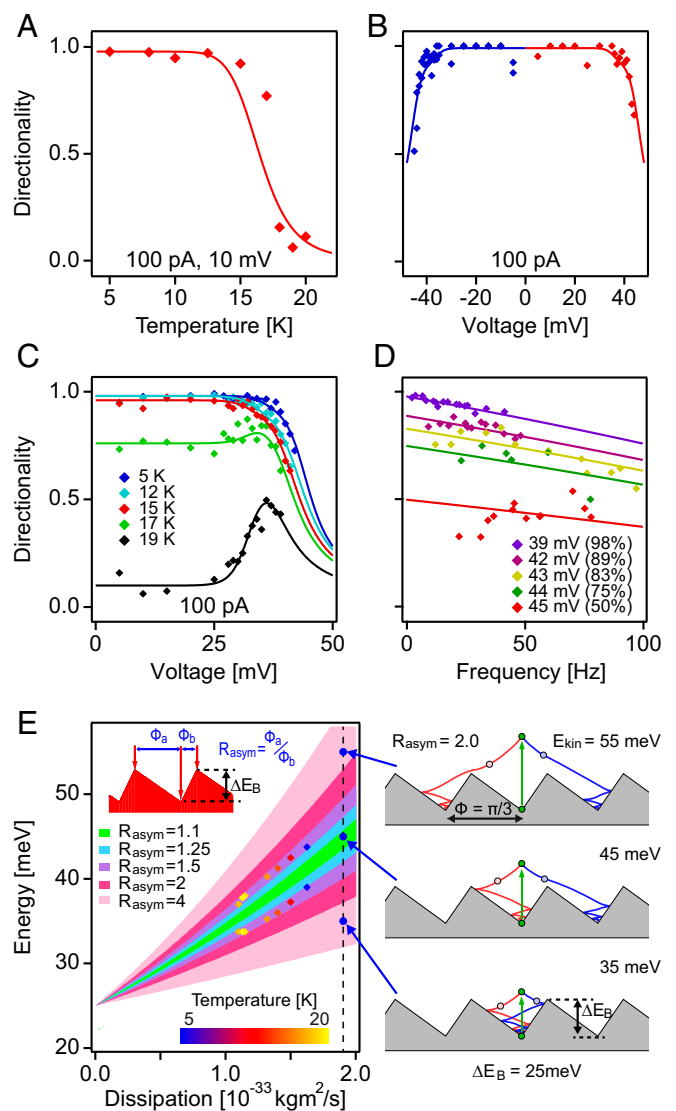

Fig. 3. Parametric dependence of the nanomotor's directionality. (*A*) Dependence of the directionality on temperature ($V_G = 10$ mV; $I_T = 100$ pA), (*B*) bias voltage for both polarities ($I_T = 100$ pA; $T = 5$ K), (*C*) bias voltage at various temperatures between 5 and 19 K ($I_T = 100$ pA), and (*D*) rotation frequency controlled via varying I_T for several V_G. In *A–D* the markers represent experimental data, while the solid lines in *A–C* are derived from the kinetic model (*SI Appendix*). The solid lines in *D* show simulated dependencies of constant directionality (given in brackets) with frequency considering finite time resolution of the experiment (*SI Appendix*). (*E*) Schematic representation of the Langevin rotation dynamics derived for ratchet potentials with $\Delta E_B = 25$ meV. (*Left*) The range of transferred kinetic energy E_{kin} for directed motion, i.e., $E_L < E_{kin} < E_R$, in dependence on energy dissipation is colored for several R_{asym}, as defined in the inset. The experimentally determined E_L and E_R are represented by two markers of the same color for several temperatures. (*Right*) The trajectories of the C_2H_2 60° rotation in a ratchet potential with $R_{asym} = 2.0$, $\lambda = 2 \times 10^{-33} \frac{\text{kgm}^2}{\text{s}}$ and $\Delta E_B = 25$ meV are displayed as a function of E_{kin}. From top to bottom: For $E_L < E_R < E_{kin}$ there is no unidirected motion, $E_L < E_{kin} < E_R$ results in directed motion by overcoming the steeper potential barrier, and $E_{kin} < E_L < E_R$ induces no rotation.

IET rotations. This increase is only effective in a narrow voltage window, above which the directionality rapidly decreases. By contrast, the I_T dependence of the directionality for a fixed voltage is weak (Fig. 3*D*), where the slight decrease with increasing current, i.e., frequency, is attributed to the detection of two rapidly successive CCW rotations as a single erroneous CW

one (solid lines in Fig. 3D). Hence we conclude that directionality stays above 95% for $|V_G| < 40$ mV even at high current.

The observation of directional motion triggered from a noncyclic, directionless, and position-independent energy input stemming from a single IET event, prompts us to apply a variant of the biased Brownian motion concept proposed by Astumian and Hänggi for modeling the underlying mechanism (28, 29). Our model of IET-induced rotation assumes a static, periodic, but asymmetric potential $U(\phi)$ ($\phi = [0,2\pi]$, with $\frac{\pi}{3}$ periodicity), with the asymmetry of the potential, R_{asym}, defined in Fig. 3E, Inset and *SI Appendix*, Fig. S11. A single IET event instantaneously excites the molecule from its ground state and its trajectory $\phi(t)$ is obtained from Langevin dynamics $I\ddot{\phi} = -\frac{\partial U(\phi)}{\partial \phi} - \lambda\dot{\phi}$, where I is the moment of inertia and λ the viscous dissipation coefficient (28, 29). Depending on R_{asym} and λ, two dissimilar minimum kinetic energies E_L and E_R are required to overcome the barrier to the left (i.e., CW) and to the right (i.e., CCW), respectively. These energies are the basis for describing frequency and directionality by the kinetic model (*SI Appendix*).

Matching this kinetic model to our experimental data in Figs. 2C and 3C allows determination of the temperature-dependent $E_L(T)$ and $E_R(T)$ which are represented by colored markers in Fig. 3E. From these values we deduce R_{asym} to be $1.25 < R_{asym} < 1.5$ assuming $\Delta E_B = 25$ meV. The reduction of the dissipation λ from about $1.6 \times 10^{-33}\frac{\text{kgm}^2}{\text{s}}$ at 5 K to around $1.1 \times 10^{-33}\frac{\text{kgm}^2}{\text{s}}$ at 20 K can be attributed to the less efficient coupling of the molecule to the substrate with increasing temperature.

Having successfully described the rich phenomenology of the over-the-barrier rotation processes in the CR, the unexpected, nearly perfect unidirectional rotation of C_2H_2 in the TR requires closer inspection. Tunneling, especially of hydrogen, is a well-established phenomenon in chemistry (30) and surface science (19), and plays a crucial role in numerous biological processes like enzyme-catalyzed reactions (31). The approximately exponential decrease of the tunneling rate with increasing mass, however, allows reasonably high tunneling rates of heavy atoms or molecules only for very small barrier heights and tunneling distances. Despite these restrictions, many tunneling transitions on surfaces involving heavy atoms like cobalt or small molecules have been reported (15, 20, 21, 32).

In this respect, the tunneling of formaldehyde (CH_2O) between two adsorption configurations on Cu(110) reported by Lin et al. is very close to the C_2H_2 rotation in terms of ΔE_B, moment of inertia, and rotation angle, and thus yields comparable frequencies ν_T (32). In both cases ν_T is critically tip-condition-dependent and varies between 0.01 and 0.1 Hz for CH_2O/Cu(110) and between 0.25 and 5 Hz for C_2H_2/Pd$_3$ surface. Thus, to evidence the strong isotopic dependence and corroborating quantum tunneling, we have paid attention that the ν_T for C_2H_2, fully (C_2D_2), and partially deuterated acetylene (C_2DH) are determined consecutively on the same sample with the same STM tip (*SI Appendix*, Fig. S15). Fig. 4A shows the resulting $I_T(t)$ sequences for C_2H_2, C_2DH, and C_2D_2 which reveal ν_T ratios (with respect to C_2H_2) of $1 : 0.56(11) : 0.24(5)$ ($C_2H_2 : C_2DH : C_2D_2$), which we consistently observe with different tips (*SI Appendix*, Table ST3 and Fig. S16). This strong relative reduction of ν_T is contrasted by the comparatively small relative change of moment of inertia $1 : 1.08 : 1.2$ and thus indicative for quantum tunneling. Careful inspection of the $I_T(t)$ sequence of C_2DH with broken C_2 symmetry reveals that the rotation cycles through six rather than three current levels (Fig. 4B), which proves that a full acetylene rotation indeed requires six CCW 60° rotations. Comparison of the experimentally determined ν_T ratios to the corresponding Wentzel–Kramers–Brillouin (WKB) tunneling frequency (*SI Appendix*) shows an excellent match for a barrier height of $\Delta E_B = 25$ meV (Fig. 4D).
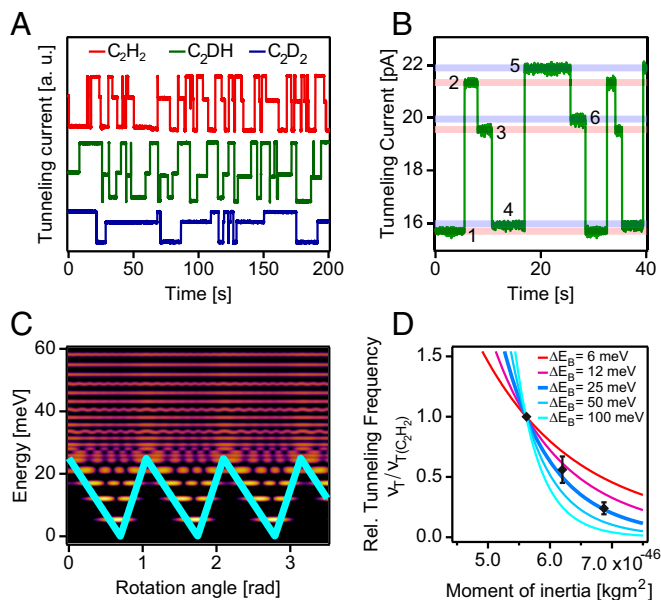

Fig. 4. Quantum tunneling rotation of acetylene. (A) $I_T(t)$ curves for C_2H_2, C_2DH, and C_2D_2, with a special focus on the six different current levels in an $I_T(t)$ curve of C_2DH in B. In C the ratchet potential is shown in turquoise, based on which the C_2H_2 quantum states, energy levels, and tunneling frequencies are determined. The color (black to yellow) represents the probability density of the quantum states. The dependence of ν_T in the WKB approximation with the moment of inertia, normalized to the ν_T at 5.62×10^{-46} kgm^2 (C_2H_2) is displayed as solid lines in D for several ΔE_B (*SI Appendix*). The black markers represent the experimental ν_T for C_2H_2, C_2DH, and C_2D_2, each normalized to the one of C_2H_2.

Quantum tunneling rotations concomitant with high directionality of 97.7% allow for an estimation of the entropy change of a single tunneling rotation from the experimental CCW and CW rotation probabilities, given by $\Delta S = -k_B \ln(p_{pCCW}/p_{CW}) \approx -k_B \ln(100/1) \approx -0.4\frac{\text{meV}}{\text{K}}$. This implies that the directional rotation in the TR must be a nonequilibrium process with energy dissipation $\Delta Q > 2$ meV at 5 K and $\Delta Q > 6$ meV at 15 K per rotation. As these values of ΔQ are on the order of the energy difference of two frustrated rotation modes of C_2H_2 (e.g., $\hbar\omega_{10} - \hbar\omega_{00} = 6.8$ meV; Fig. 4C and *SI Appendix*, Fig. S14 and Table ST2), one might assume that the required nonequilibrium tunneling proceeds via an excitation from the ground state to a bound rotational mode as proposed by Nacci et al. (21). We estimate a maximum power dissipation of 100 meV/s per motor, assuming 10-Hz tunneling frequency as upper bound. On the other hand, the STM required for monitoring the rotation, locally dissipates at least 3×10^6 meV/s even at the lowest settings of 1-pA tunneling current and 0.5-mV bias. We still observe the constant rotation frequency with persisting high directionality at such extreme settings. Therefore, the STM tip is presumably critical in driving the system out of equilibrium also in the regime of tunneling motion.

In conclusion, the highly directional tumbling rotation of C_2H_2 on the chiral PdGa{111}Pd$_3$ surfaces exhibits a rich phenomenology, most prominently characterized by an unprecedentedly high directionality and small motor size. Its rotor (C_2H_2) and stator (Pd$_3$-Ga$_6$-Pd$_3$ cluster) shown in Fig. 1A comprise just 16 atoms to form a unidirectional six-state cyclic molecular motor (Fig. 4B) through all of which it cycles ceaselessly, powered exclusively by single electrons. This contrasts reported motors driven by light or chemical reactions, since for the former concerted thermal and light-driven activation is required. The latter usually requires a cycling of the chemical environment to complete

one cycle. In the classical regime, we could establish a Langevin kinetic model of the motion describing frequency and directionality with temperature, STM bias voltage, and tunneling current. The model provides robust values for the rotational potential asymmetry R_{asym} and the temperature dependence of the viscous dissipation coefficient $\lambda(T)$ relating the operation of this molecular machine to atomic friction. The negative entropy change associated with the high rotation directionality, also observed in the tunneling regime, challenges the understanding of this simple cyclic machine in terms of dissipative quantum tunneling dynamics (33). In the future, it might be possible to convert energy via forced excitations, e.g., optical, or by IET, into directional motion and thus investigating energy harvesting at the smallest possible length scale.

Materials and Methods

All experiments were performed under ultrahigh vacuum conditions with a base pressure below 5×10^{-11} mbar using an Omicron low-temperature STM operated at 5 K. The measurements were performed with different tips including 80:20 Pt/Ir tip, Tungsten STM, and Tungsten Q+ Sensor tips. We have found no systematic difference in the experimental results obtained with different tips. The PdGa crystal surface was prepared by repeated sputter and annealing cycles (sputtering: Ar$^+$, 1 keV; annealing: 20 min at 870 K).

Before dosing C_2H_2, which was purchased from PanGas with a purity of 99.6%, the gas line was precleaned by purging with the gas or by freeze–thaw cycling (77 K). In case of C_2D_2, purchased from CDN isotopes with 99% purity (C_2DH being the impurity), no precleaning was performed, because the gas was bottled with atmospheric pressure. Both gases were dosed by chamber backfilling through a leak valve at a pressure of 2×10^{-9} mbar. By removing the sample from the STM stage at 5 K exposing it to the acetylene outside the cryostat for a short time (generally 10–20 s) the most effective exposure conditions were achieved.

1. R. P. Feynman, There's plenty of room at the bottom. *Eng. Sci.* **23**, 22–36 (1960).
2. D. M. Eigler, E. K. Schweizer, Positioning single atoms with a scanning tunnelling microscope. *Nature* **344**, 524–525 (1990).
3. N. Koumura, R. W. J. Zijlstra, R. A. van Delden, N. Harada, B. L. Feringa, Light-driven monodirectional molecular rotor. *Nature* **401**, 152–155 (1999).
4. K. Svoboda, C. F. Schmidt, B. J. Schnapp, S. M. Block, Direct observation of kinesin stepping by optical trapping interferometry. *Nature* **365**, 721–727 (1993).
5. M. Schliwa, G. Woehlke, Molecular motors. *Nature* **422**, 759–765 (2003).
6. V. Balzani *et al.*, Autonomous artificial nanomotor powered by sunlight. *Proc. Natl. Acad. Sci. U.S.A.* **103**, 1178–1183 (2006).
7. D. Roke, S. J. Wezenberg, B. L. Feringa, Molecular rotary motors: Unidirectional motion around double bonds. *Proc. Natl. Acad. Sci. U.S.A.* **115**, 9423–9431 (2018).
8. J. V. Hernández, E. R. Kay, D. A. Leigh, A reversible synthetic rotary molecular motor. *Science* **306**, 1532–1537 (2004).
9. S. Erbas-Cakmak *et al.*, Rotary and linear molecular motors driven by pulses of a chemical fuel. *Science* **358**, 340–343 (2017).
10. H. L. Tierney *et al.*, Experimental demonstration of a single-molecule electric motor. *Nat. Nanotechnol.* **6**, 625–629 (2011).
11. T. Kudernac *et al.*, Electrically driven directional motion of a four-wheeled molecule on a metal surface. *Nature* **479**, 208–211 (2011).
12. Y. Zhang *et al.*, A chiral molecular propeller designed for unidirectional rotations on a surface. *Nat. Commun.* **10**, 3742 (2019).
13. S. Kassern *et al.*, Artificial molecular motors. *Chem. Soc. Rev.* **46**, 2592–2621 (2017).
14. C. Pezzato, C. Cheng, J. F. Stoddart, R. D. Astumian, Mastering the non-equilibrium assembly and operation of molecular machines. *Chem. Soc. Rev.* **46**, 5491–5507 (2017).
15. A. J. Heinrich, C. P. Lutz, J. A. Gupta, D. M. Eigler, Molecule cascades. *Science* **298**, 1381–1387 (2002).
16. U. G. Perera *et al.*, Controlled clockwise and anticlockwise rotational switching of a molecular motor. *Nat. Nanotechnol.* **8**, 46–51 (2013).
17. G. J. Simpson, V. García-López, A. Daniel Boese, J. M. Tour, L. Grill, How to control single-molecule rotation. *Nat. Commun.* **10**, 4631 (2019).
18. B. C. Stipe, M. A. Rezaei, W. Ho, Coupling of vibrational excitation to the rotational motion of a single adsorbed molecule. *Phys. Rev. Lett.* **81**, 1263–1266 (1998).
19. L. J. Lauhon, W. Ho, Direct observation of the quantum tunneling of single hydrogen atoms with a scanning tunneling microscope. *Phys. Rev. Lett.* **85**, 4566–4569 (2000).
20. J. A. Stroscio, R. J. Celotta, Controlling the dynamics of a single atom in lateral atom manipulation. *Science* **306**, 242–247 (2004).
21. C. Nacci *et al.*, Current versus temperature-induced switching in a single-molecule tunnel junction: 1,5 cyclooctadiene on Si(001). *Nano Lett.* **9**, 2996–3000 (2009).
22. K. Sun *et al.*, Supramolecular motors on graphite surface stabilized by charge states and hydrogen bonds. *ACS Nano* **11**, 10236–10242 (2017).
23. D. Rosenthal *et al.*, Surface investigation of intermetallic PdGa($\overline{111}$). *Langmuir* **28**, 6848–6856 (2012).
24. J. Prinz, O. Gröning, H. Brune, R. Widmer, Highly enantioselective adsorption of small prochiral molecules on a chiral intermetallic compound. *Angew. Chem. Int. Ed. Engl.* **54**, 3902–3906 (2015).
25. J. Prinz *et al.*, Isolated Pd sites on the intermetallic PdGa(111) and PdGa(-1-1-1) model catalyst surfaces. *Angew. Chem.* **124**, 9473–9477 (2012).
26. J. Prinz *et al.*, Adsorption of small hydrocarbons on the three-fold PdGa surfaces: The road to selective hydrogenation. *J. Am. Chem. Soc.* **136**, 11792–11798 (2014).
27. S. Gao, M. Persson, B. I. Lundqvist, Theory of atom transfer with a scanning tunneling microscope. *Phys. Rev. B* **55**, 4825–4836 (1997).
28. R. D. Astumian, S. Mukherjee, A. Warshel, The physics and physical chemistry of molecular machines. *ChemPhysChem* **17**, 1719–1741 (2016).
29. P. Hänggi, F. Marchesoni, Artificial Brownian motors: Controlling transport on the nanoscale. *Rev. Mod. Phys.* **81**, 387–442 (2009).
30. P. R. Schreiner, Tunneling control of chemical reactions: The third reactivity paradigm. *J. Am. Chem. Soc.* **139**, 15276–15283 (2017).
31. J. P. Klinman, A. Kohen, Hydrogen tunneling links protein dynamics to enzyme catalysis. *Annu. Rev. Biochem.* **82**, 471–496 (2013).
32. C. Lin, E. Durant, M. Persson, M. Rossi, T. Kumagai, Real-space observation of quantum tunneling by a carbon atom: Flipping reaction of formaldehyde on Cu(110). *J. Phys. Chem. Lett.* **10**, 645–649 (2019).
33. A. O. Caldeira, A. J. Leggett, Influence of dissipation on quantum tunneling in macroscopic systems. *Phys. Rev. Lett.* **46**, 211–214 (1981).

Supplementary Materials for

Molecular motor crossing the frontier of classical motion to quantum tunneling motion

Samuel Stolz, Oliver Gröning, Jan Prinz, Harald Brune, Roland Widmer

Correspondence to: oliver.groening@empa.ch

This PDF file includes:

> Supplementary Text
> Figs. S1 to S16
> Tables ST1 to ST3
> Captions for Movies SV1

Other Supplementary Materials for this manuscript include the following:

> Movies SV1

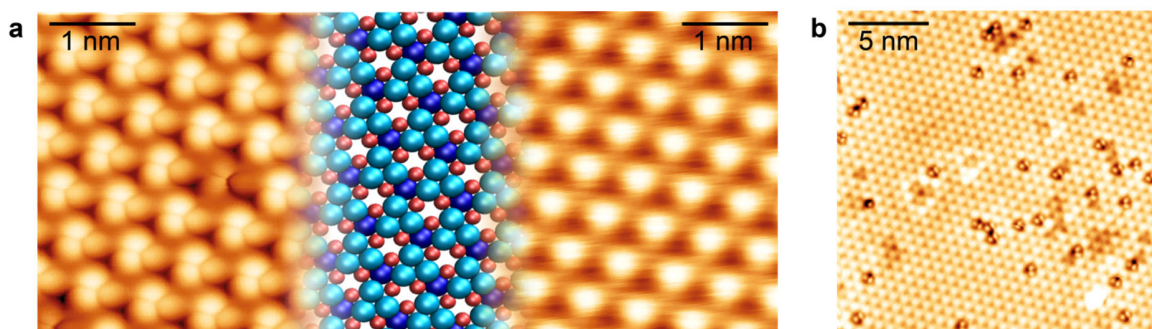**STM images of clean Pd$_3$ surfaces and with C$_2$H$_2$ adsorbed**

Fig. S1

a STM images of the clean Pd$_3$ surface recorded at 5 K, 10 mV and 200 pA to resolve the Pd trimers in the top layer (left) partially overlaid by the atomic structure (center) and recorded at 77 K, -200 mV and 200 pA (right), representing the normal STM images taken. **b** 20 x 20 nm^2 STM image of C$_2$H$_2$ adsorbed on Pd$_3$, visualizing the usual coverage we worked with (5 K, 5 mV, 100 pA).

Voltage and current dependence of the rotation frequency in the tunneling regime

For temperatures $T < 15\ K$ and bias voltages $|V_G| \leq 30\ mV$ the rotation frequency ν_T shows a pronounced dependency on the tip condition and can vary between approximately 0.1 Hz and 5 Hz, which is not uncommon for tunneling transition rates. When ν_T is high, we detect a rotation frequency, which is independent of voltage and only weakly dependent on the current. Such an example is depicted in Fig. S2 for tip condition 1, where increasing the current from 2 pA to 200 pA only increases ν_T from 2 Hz to 5 Hz.

If the base frequency is low a transition from a voltage independent and weakly current dependent region at low currents to a linear current dependence and strong voltage dependence at higher currents can be observed as shown again in Fig. S2 for tip condition 2.
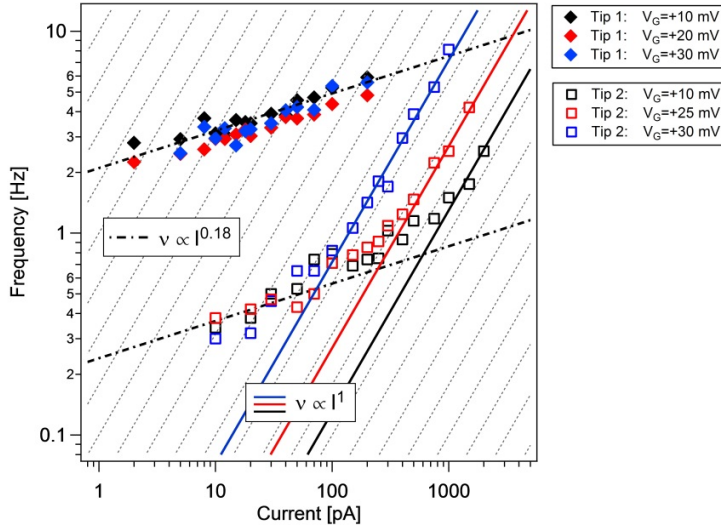

Fig. S2

Experimentally measured rotation frequencies (markers) as a function of current for different tip conditions and different STM bias voltages.

Such transitions are characteristic for vibrationally assisted tunneling (VAT) as proposed by Ueba *et al.* (1) The linear part corresponds to tunneling from excited vibrational states populated by energy transfer from inelastic electron tunneling. The weakly current dependent region would correspond to deep tunneling from the vibrational ground state. The fact that there is still a weak current dependence can be attributed to the fact that tunneling current and tip height cannot be varied independently, but are related via:

$$I_T(z) \propto e^{-\frac{2}{\hbar}\sqrt{2m_e\Phi}z} \approx e^{-2.3z[\text{Å}]}$$

for bias voltages much smaller than the work function $\Phi = 5\ eV$. A variation of the tunneling current over 2 orders of magnitude would therefore correspond to a change in the tip height of about 2 Å. It is plausible that the tip softens the potential energy landscape and thereby the tunneling rate is increased. In the case of very close proximity of the tip to the substrate, the potential landscape can be significantly altered, as the attractive interaction between tip and molecule becomes more important. Figure S3 illustrates this situation, where the residence time of

the acetylene in the rotation state furthest from the tip is dramatically reduced. Nevertheless, a very high degree of directionality of 91% is maintained.

"With regard to the VAT mechanism, the theoretical tunneling frequency for the vibrational ground state ($\hbar\omega_{00} = 3.58\ meV$, see chapter Determination of the tunnel splitting ΔE_T and the tunneling frequency ν_{Th})"

) would be 12.95 MHz compared to 571.9 MHz (first excited vibration $\hbar\omega_{10} = 10.57\ meV$) and 10'150 MHz (second excited vibration $\hbar\omega_{20} = 16.54\ meV$).
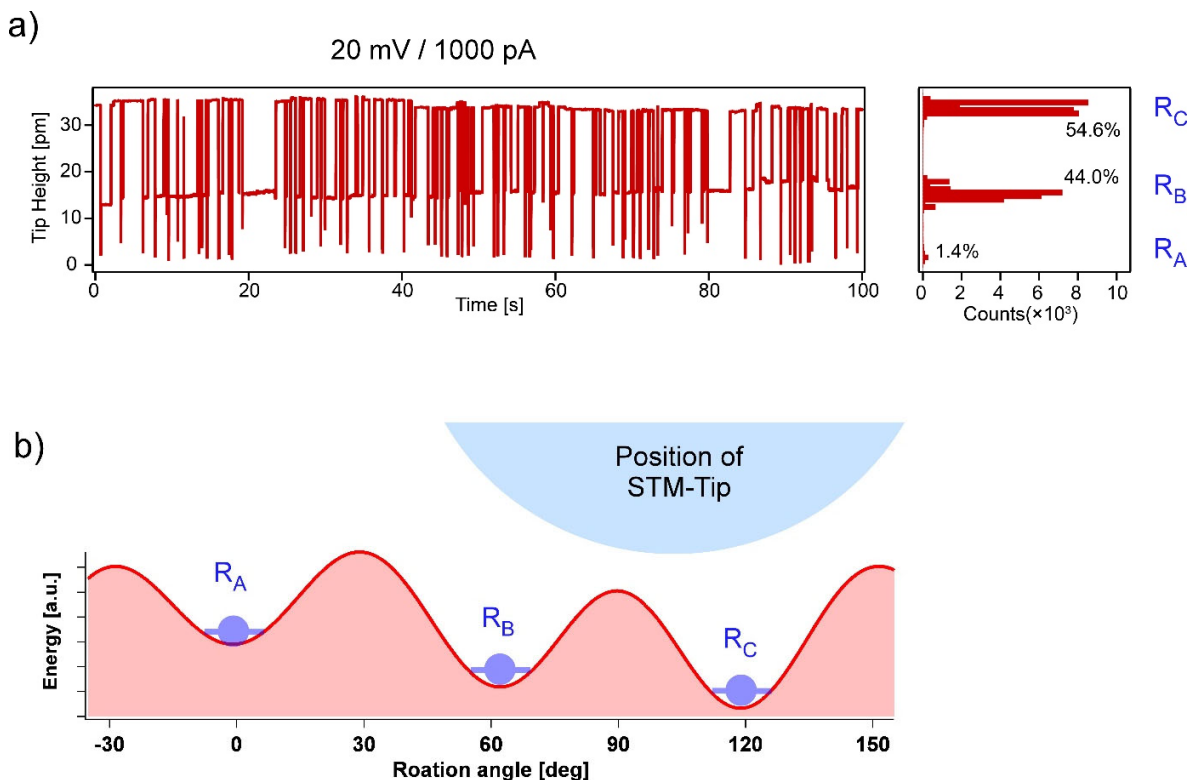
a)

b)

Fig. S3

a Constant current tip-height time series of the C_2H_2 rotation at very high tunneling current of 1 nA. On the right, the histogram of the rotation states with the corresponding residence probability is shown. **b** Schematic illustration of how the STM tip position (indicated by the light blue hemisphere) can might an asymmetry in the potential energy landscape (red curve) of the C_2H_2 rotation. The depicted situation assumes an additional extended attractive tip-C_2H_2 interaction when the tip is in very close proximity to the surface, which is the case for high current – low bias setpoints.

Details of the rotational motion

Figure S4a shows a series of constant current STM topography images with the three rotation states 1 to 3 observed for the acetylene molecule in the sequence of their motion from left to right. The atomic structure of the substrate has been superimposed to the STM images. As can be seen from Figure S4b the acetylene molecule does not simply rotate around the center of the Pd trimer, but performs a combination of rotation and translation, i.e. a tumbling rotation. 1 and 1' represent a 180° rotation of the C_2H_2 which are indistinguishable due to the C_2 symmetry of the molecule.
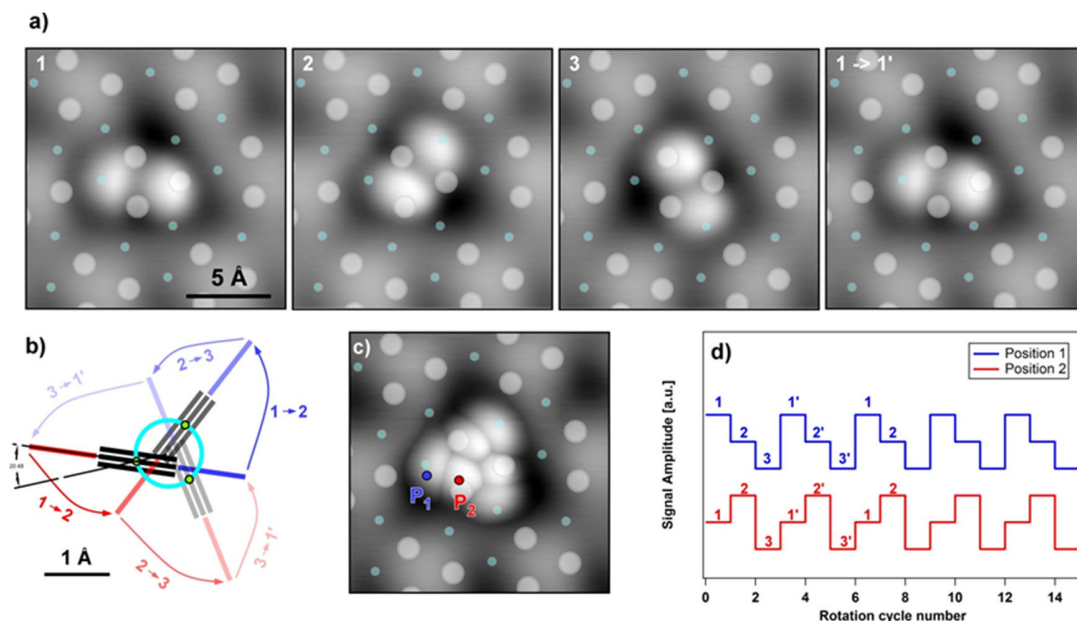

Fig. S4

a Series of STM images of C_2H_2 on Pd_3 with the surface structure superimposed. 1-3 shows the acetylene's three distinguishable rotation states. **b** The assumed motion of acetylene on the Pd_3 surface. **c** Superposition $(z(x,y) = max(z_1(x,y), z_2(x,y), z_3(x,y)))$ of the three rotation states shown in **a**. **d** Schematic $I_T(t)$ spectra for the two accordingly colored tip positions marked in **c**.

Simulation of jump sequence maps

In order to compare the experimentally measured jump sequence maps with an idealized model of the acetylene motion, we describe the STM signal (current or height) by three amplitude functions $I_i(x, y), i = \{1,2,3\}$, one for each distinguishable rotation state. The STM signal, for a given rotation state of the molecule, can be reasonably well approximated by the superposition of two ellipsoidal Gaussian peaks positioned at the two lobes of the acetylene molecule. This leads to the following approximation of the STM signature:

$$I_i(x, y) = \exp(\sigma_1(x - x_i)^2 + \sigma_2(y - y_i)^2) + \exp(\sigma_1(x + x_i)^2 + \sigma_2(y - y_i)^2)$$

The parameters σ_1 and σ_2 define the size and ellipticity of the lobes L_1 and L_2, separated by the distance d (Figure S5a). Variations in σ_1 and σ_2 are assumed to be due to changes in bluntness and symmetry of the STM tips only. Off-center positions and rotations are then realized by the appropriate translation and rotation operations on the coordinate system, as sketched in Figure S5a, where M_1 represents the center of the Pd trimer and M_2 the center of mass of C₂H₂. r corresponds to the distance between M_1 and M_2, while φ_1 is the angle between the vectors connecting M_1 to M_2 and M_1 to the center of a neighboring Pd trimer. Finally φ_2 is the angle by which the molecule is tilted with respect to the vector $\overrightarrow{M_1M_2}$. The functions I_i, $i = \{1,2,3\}$, are related by a 3-fold rotation symmetry regarding the lobe positions. All variables, r, d, φ_1 and φ_2 are chosen, such that the resulting amplitude distribution of the lobes fit well with the experimental STM image of a single molecule as seen in Figure S5b. This way we determine $r = 0.55 \pm 0.1$ Å, $d = 3.25 \pm 0.2$ Å, $\varphi_1 = 5°$ and $\varphi_2 = 20°$.
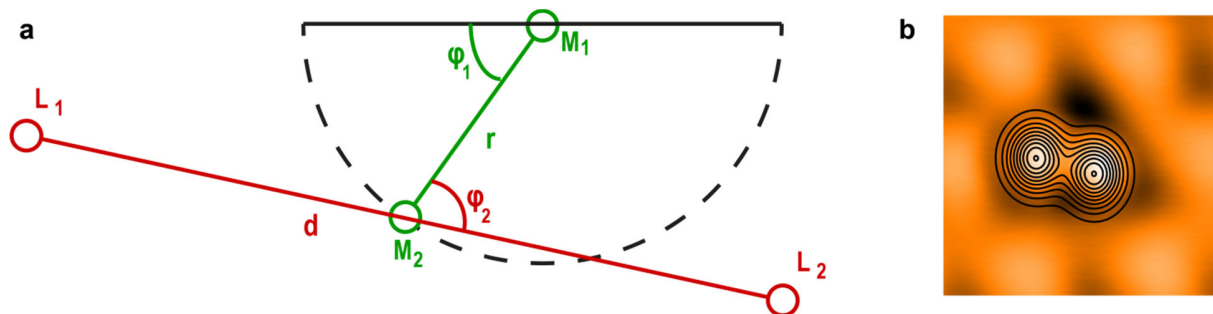

Fig. S5

a Sketch of the C₂H₂ on Pd₃ system and parameters used for the simulation of the jump sequence maps. **b** Simulated C₂H₂ STM image overlaid as contours on an experimental STM image.

With the synthetic model for the spatial current in the three rotational configurations $I_i(x, y)$, $i = \{1,2,3\}$ the time sequence of current level $I_T(x, y, t)$ can be obtained for any tip position and any cycle sequence (in our case the CCW one $... \rightarrow 1 \rightarrow 2 \rightarrow 3 \rightarrow 1 (1') \rightarrow \cdots$) correspondingly the ascending (red) or descending current stair case (blue, see Fig. S4d) can be determined at any position. It needs to be stressed that while the sequence can be determined in the model for arbitrarily small current jumps, in the experiment this is not the case. If the current variation between different rotational configurations becomes too small, e.g. far away from the molecule or where two current levels become degenerate, the directionality goes to 0 in the experiment. In the

model we have taken this into account by fading the directionality value when the smaller current jump is below 10% of the current amplitude ($max(I_L, I_R)$).

The effect of the variables r and φ_2 on the superimposed current and jump sequence maps is demonstrated in Fig. S6a-f. If the molecule would symmetrically rotate around its center of gravity (i.e. $r = 0$) the 6-fold symmetric pattern of Fig. S6a and d would emerge. Allowing for an off-center rotation $r = 0.5$ Å but without tilt $\varphi_2 = 0$ the 3-fold symmetric pattern of Fig. S6b and e result. Considering an off-center rotation with tilt $\varphi_2 = 20°$, shown in Fig. S6c and f, reproduces well the slightly chiral pattern of the experiment.

The jump sequence maps are very sensitive to the imaging conditions and can appear significantly different as illustrated in Fig. S7. While the experimental jump sequence map in Fig. S7c was recorded with a rather blunt, but symmetric tip described by $\sigma_1 = \sigma_2 = 0.25$ Å^{-1} , the tip with which the experimental jump sequence map in Fig. S7f was recorded was sharper, but asymmetric, best described with $\sigma_1 = 0.45$ Å^{-1} and $\sigma_2 = 0.35$ Å^{-1}, respectively, resulting in an asymmetric jump sequence map.
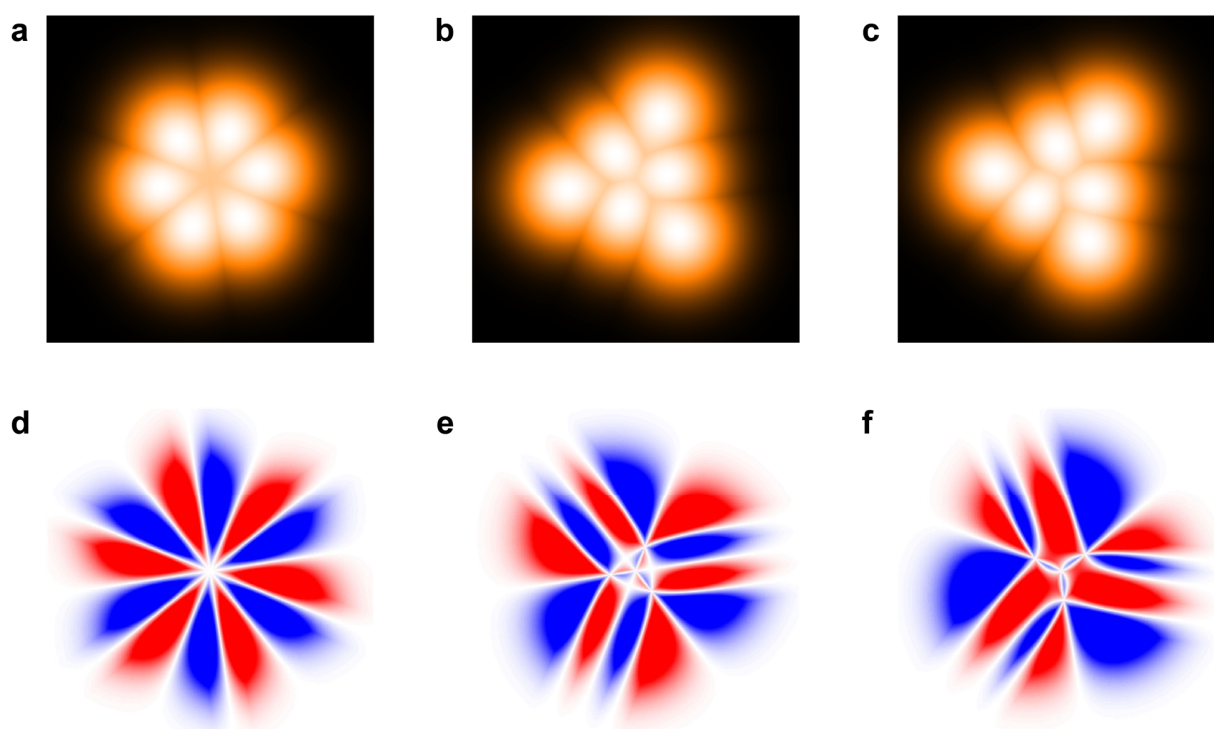

Fig. S6

a-c Simulated, superimposed current maps $(I(x,y) = max(I_1(x,y), I_2(x,y), I_3(x,y)))$ for different rotational motions with the corresponding jump sequence maps shown in **d-f**.
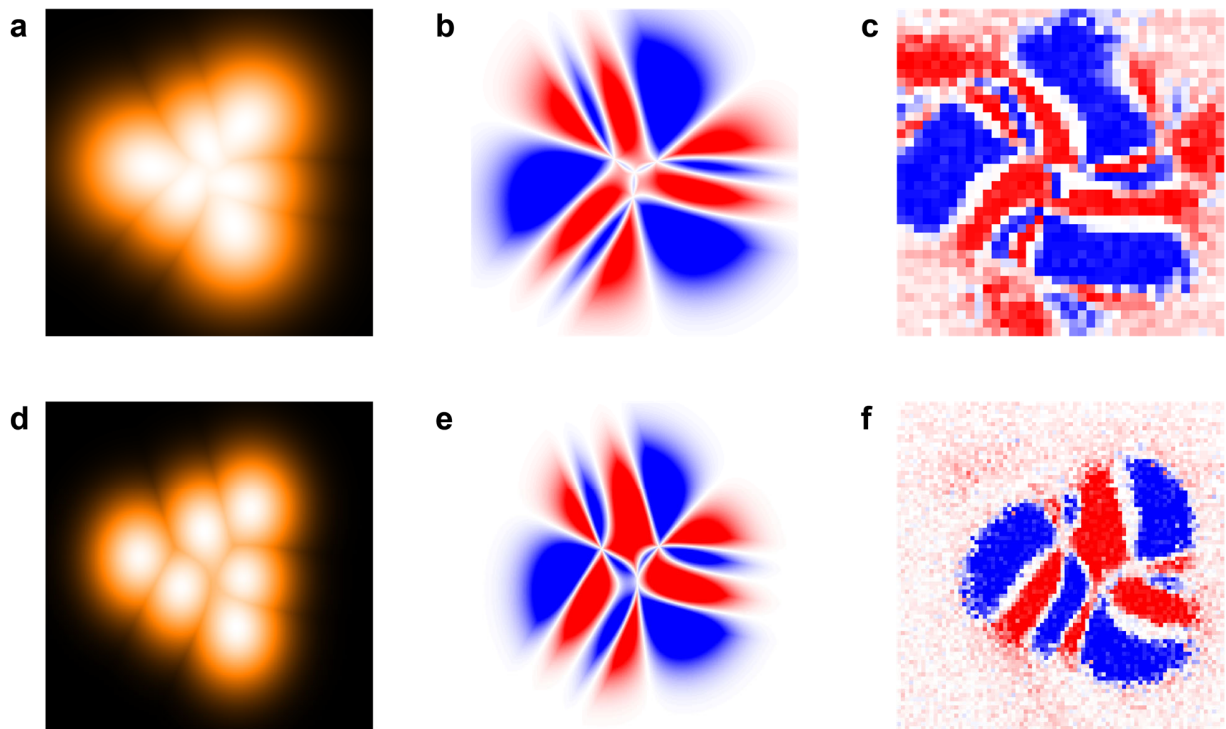
Fig. S7

Superimposed current maps in **a** and **d**, with the corresponding optimized simulated jump sequence maps in **b** and **e**, and the experimental jump sequence maps shown in **c** and **f** for two different STM tips and experimental conditions. (**c** 38x38 points equidistant grid, const. height map $25 \, pA < I_T < 110 \, pA$, $V_G = 10 \, mV$; **f** 80x80 points equidistant grid, const. current map, $I_T = 100 \, pA$, $V_G = 10 \, mV$).

Statistical analysis of the configurational residence times

Based on the grid of the 6400 z(x,y,t) time series, recorded with 10 mV and 100 pA, which is shown in Fig. S7f and Fig. 2e of the main text we have analyzed the residence times of the rotor in the different configurations. For this analysis we have considered all time series with directionality larger than 80% (a total of 1382) shown by the yellow markers in Fig. S8a. The criterion on the directionality has been chosen to select $z_T(t)$ with sufficiently reliable automatic rotation detection.
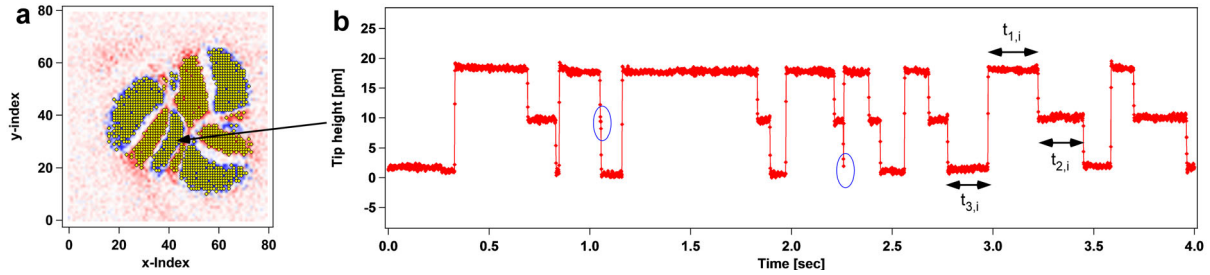

Fig. S8

a Jump sequence map with the yellow markers denoting the positions of the $z_T(t)$ time series considered for the statistical analysis. **b** z(t) at the position marked by the arrow.

The $z_T(t)$ sequence shown in Fig. S8b illustrates the difficulty of the automatic rotation detection. For this sequence the algorithm has detected 20 CCW and 2 CW jumps resulting in a directionality of 91%. However, closer inspection of the CW jumps, marked by the blue ellipses in Fig. S8b, visualizes that these are very short double jumps in the CCW direction. This means there are in fact 24 CCW and 0 CW rotations with a directionality of 100%.

Analysis of the 26295 rotation events shows the following distribution of the residence time for the different rotation states.
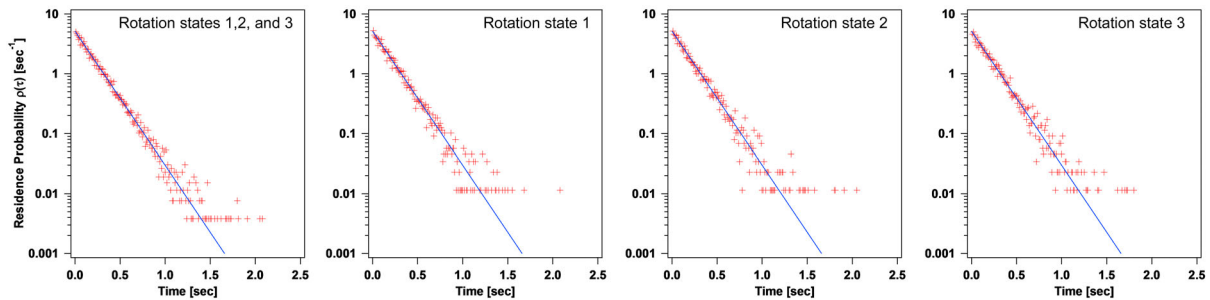

Fig. S9

Residence probability distribution for all rotation states combined and individual. The blue solid line in all figures corresponds to $\rho(\tau) = \lambda^{-1}\exp(-\tau\lambda^{-1})$ with λ=0.194 sec denoting the rotation time constant.

Figure S9 proves that the residence or persistence times in the different rotation states follow the same Poisson process distribution with the same time constant. The rotation events are therefore independent stochastic processes with a homogenous differential probability $d\rho = -\lambda^{-1}\rho d\tau$. The mean frequency for this tip condition is $\nu = \frac{1}{\lambda} = 5.15\ Hz$.

9

As shown in Fig. S10, we find a weak dependence of the time constant with the tip position, where rotation frequency decreases from approx. 6.2 Hz in the center of the motor to 4.5 Hz at a distance of 4 Å from the center.
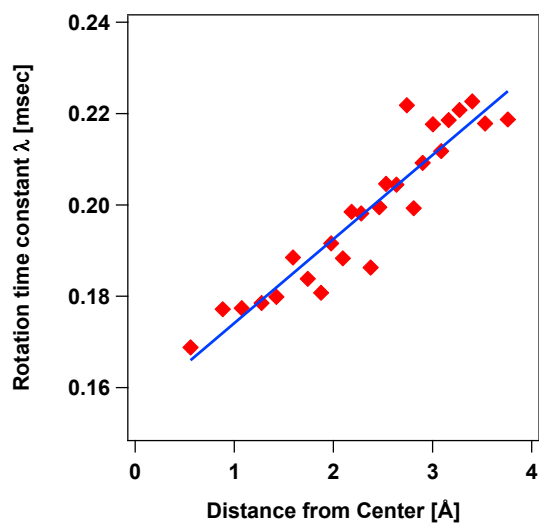

Fig. S10

Rotation time constant λ as a function from the distance from the center.

Langevin dynamics of the rotation

To describe the motion of the C_2H_2 in the classical regime we rely on the Langevin rotational equation of motion in an asymmetric saw-tooth potential with a period of $\pi/3$.

$$I\ddot{\phi} = -T_n - \lambda\dot{\phi} \quad (1)$$

Where I denotes the moment of inertia ($I = 5.62 * 10^{-46}\ kgm^2$ for C_2H_2 in our case), T_n the restoration torque (with $n = \{CW, CCW\}$) and λ_v the dissipation coefficient.
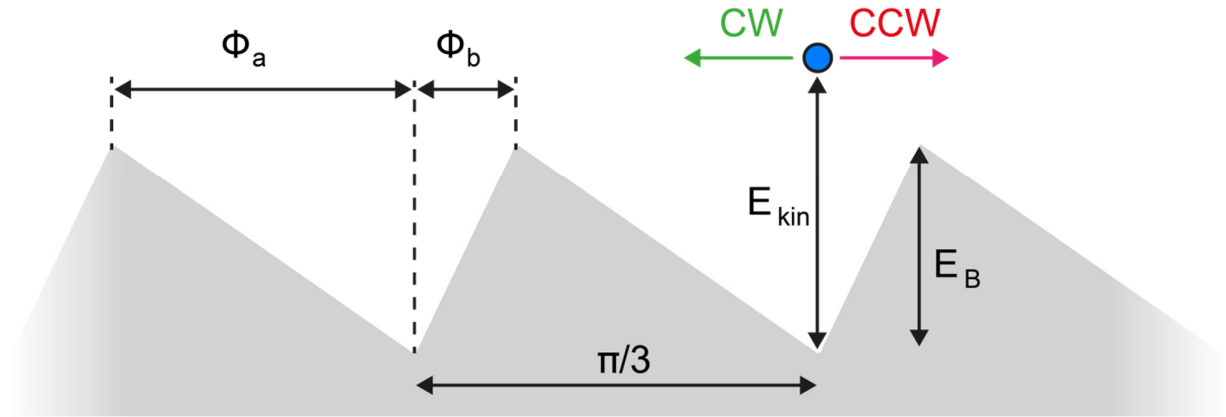

Fig. S11

Schematic representation of the rotational motion in an asymmetric saw-tooth potential.

Due to the asymmetry of the potential the particle moving with a certain kinetic energy will experience a different restoration torque if it moves left or right, $T_{CW} = \frac{E_B}{\phi_a}$ and $T_{CCW} = \frac{E_B}{\phi_b}$, respectively. Equation (1) has the following general solution

$$\phi(t) = -\frac{A}{B}t + c_1\frac{\exp(Bt)}{B} + c_2$$

With $A = -\frac{E_B}{\phi_a I}$ for moving left and $A = -\frac{E_B}{\phi_b I}$ for moving right and $B = -\frac{\lambda_v}{I}$.

For a given initial kinetic energy E_{kin} and assuming a starting position at rest in the minimum of the potential well $\phi(0) = 0$ we find:

$$\dot{\phi}(0) = \sqrt{2E_{kin}/I}$$

$$c_1 = \dot{\phi}(0) + \frac{A}{B} \quad \text{and} \quad c_2 = -\frac{c_1}{B}$$

The time of the molecule to travel to the extreme extend is then given by $\dot{\phi}(t_{ex}) = 0$ and yields

$$t_{ex} = \frac{1}{B}\ln(\frac{A}{Bc_1})$$

The condition that the particle will jump to the next well is then given by the condition:

$$\phi(t_{ex}) > \phi_a \ or \ \phi_b$$

The relations:

$$\phi(t_{ex}(E_{kin}^{CW})) = \phi_a$$

$$\phi(t_{ex}(E_{kin}^{CCW})) = \phi_b$$

yield the minimum initial kinetic energy for a clock-wise rotation E_{kin}^{CW} and counter-clockwise rotation E_{kin}^{CCW}. These energies depend on I, E_B, R_{asym} and λ_v as shown in Fig. 3d of the main manuscript.

Modelling the voltage-temperature dependent rotation frequency and directionality

Like for many other molecule manipulations using STM (several listed in Ref. (2)), we can induce rotations via inelastic electron tunneling (IET), although we have no direct proof of C₂H₂ to exhibit any vibration or libration mode in the relevant energy range. Our model is similar to "action spectroscopy" proposed by Kim et al (2), but they never discussed how this might lead to directed motion.

We simply assume, that the transferred energy from electron to molecule must be at least E_L to overcome the steeper potential barrier of the ratchet potential and $E_R > E_L$ to overcome the other potential barrier. We assume the probability to overcome the potential barrier on the steeper p_L or shallower p_R side to be an error function

$$p_{L/R}(V) = c * \left(\frac{1}{2} + \frac{1}{2} \mathrm{erf} \left(\frac{|V| - E_{\frac{L}{R}}}{\alpha} \right) \right)$$

With α describing the broadening of the error function due to non-zero temperature or electric noise of the STM and c the probability that an IET transfers enough energy for a tunneling event to occur. The IET induced frequency ν_L and ν_R in either direction is determined by

$$\nu_{L/R}(V) = \int_0^V c N_{IET} \left(\frac{1}{2} + \frac{1}{2} \mathrm{erf} \left(\frac{|V'| - E_{L/R}}{\alpha} \right) \right) dV'$$

Where N_{IET} is the number of electrons tunneling between tip and sample per second. In order to compare this model to the experimentally determined rotation ν_{exp} we assume all, tunneling frequency ν_{Tunnel}, thermally induced frequency ν_{Therm}, and IET activated frequencies $\nu_{R/L}$, to be additive

$$\nu_{Exp}(V,T) = \nu_{Tunnel} + \nu_{Therm}(T) + \nu_L(V,T) + \nu_R(V,T)$$

and the directionality dir to be described by

$$dir(V,T) = \frac{0.98 \nu_{Tunnel} + \nu_L(V,T) - \nu_R(V,T)}{\nu_{exp}}$$

Considering the experiment series performed at different temperatures, but all with $I_T = 100\ pA$, thus $N_{IET} = 6.2 * 10^{11} \frac{e^-}{s}$, we find $c = 2.7 * 10^{-12}$ to be temperature independent, but α to increase from $\alpha_{5K} = 3.1\ meV$ at 5 K to $\alpha_{19K} = 3.6\ meV$ at 19 K. Furthermore, we determine $E_L = 39\ meV$ and $E_R = 43.75\ meV$ at 5 K, which, when compared to the Langevin dynamics for a ratchet potential barrier with $\Delta E_B = 25\ meV$ barrier height, results in a ratchet asymmetry $R_{asym} \approx 1.25$ and a dissipation $\lambda = 1.6 * \frac{10^{-33} kg m^2}{s}$. E_L and E_R decrease with increasing temperature, but while this leads to only marginal variations in R_{asym} between $1.25 < R_{asym} < 1.5$ for all temperatures, λ decreases from $\lambda_{5K} = 1.6 * 10^{-33} \frac{kg m^2}{s}$ at 5 K to $\lambda_{20K} = 1.1 * 10^{-33} \frac{kg m^2}{s}$ at 20 K, as seen in Fig. 3e of the main text.

Applying a modulation voltage

The presented model can further be extended to take into account a modulation voltage V_{mod}, which in our case is sinusoidal $V_{mod} = V_0 sin(f_{mod}t)$ with a modulation frequency f_{mod}. If we assume the $I_T(t)$ curve to be recorded for much longer times than $1/f_{mod}$, we can approximate the voltage distribution V_{dist} of V_{mod} to be

$$V_{dist}(V) = \sin^{-1}\frac{V}{V_0}$$

and the resulting voltage dependence of the rotation frequency $v_{mod_{L/R}}$ by the convolution of $V_{dist}(V)$ and $v_{R/L}$

$$v_{mod_{L/R}}(V) = \int V_{dist}(V') * v_{L/R}(V')dV'.$$

The model of how to treat the modulation voltage leads to a reasonable fit with experimental data as presented in Fig. S12, and thus excluding electrical noise from STM to be driving the rotation in the tunneling regime.

Another, simpler approach to predict the influence around the onset of the IET induced rotation frequencies, is to take into consideration that V_{mod} around the onset only influences the rotation frequency if the absolute value of the total voltage $|V_{tot}| = |V_{Gap} + V_{mod}|$ increases. Therefore, estimating the mean value $\bar{V}_{mod}$ of all values of V_{mod} which increase $|V_{tot}|$ is enough to describe the influence of V_{mod} on the rotation frequency around the aforementioned onset (the onset is then shifted by $\bar{V}_{mod}$ towards lower bias voltages). In case of $V_0 = 10\ mV$ we find

$$\bar{V}_{mod} = \frac{\int_0^\pi \sin(\frac{V}{V_0})dV}{\int_0^\pi dV} = \frac{2}{\pi}V_0 = 6.4meV$$

corresponding well, to what we observe experimentally, as indicated by the black lines in Fig. S12.
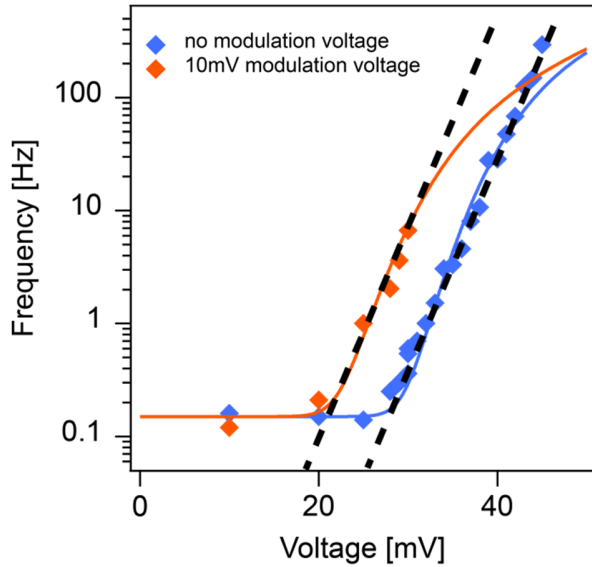
Fig. S12

Rotation frequency dependence on bias voltage if no modulation voltage (blue) or 10 mV sinusoidal modulation voltage (orange) is applied. The markers represent the experimentally determined rotation frequencies, while the solid lines are derived using equation for $v_{mod_{R/L}}$. The dashed lines indicate the increase of v for each curve, which is shifted by 6.4 mV to lower bias voltage, if a 10 mV sinusoidal modulation voltage is applied.

Influence of finite time resolution on the determination of the directionality

The probability p_J of acetylene to perform a rotation within the time interval Δt, i. e., the experimental time resolution, is assumed (and shown via the statistical analysis of the residence times in Fig. S8-9) to be stochastic, thus independent of any previous events

$$p_J = v * \Delta t$$

with v being the experimental rotation frequency.

We define the probability for a counter-clockwise (CCW) rotation as α, and thus can estimate the probability of a single CCW and clockwise (CW) rotation, p_{CCW} and p_{CW} respectively, within Δt to be $p_{CCW} = \alpha * p_J$ and $p_{CW} = (1 - \alpha) * p_J$. The directionality, assuming no jumps missed due to limited time resolution, is given by $dir_0 = \frac{p_{CCW} - p_{CW}}{p_{CCW} + p_{CW}} = 2\alpha - 1$.

Due to the limited time resolution Δt, we cannot neglect the possibility of detecting two CCW rotations as one CW ($p_{2CCW} = (\alpha p_J)^2$) or vice versa ($p_{2CW} = (1 - \alpha)^2 p_J^2$) and neither the one of detecting a CCW and a CW rotation as none ($p_{CCWCW} = \alpha(1 - \alpha)p_J^2$). Due to all these undetected rotation events, the experimentally determined directionality dir_{exp} differs from dir_0 and can be estimated to be

$$dir_{exp} = \frac{(p_{CCW} - 2p_{2CCW} + p_{2CW} - 2p_{CCWCW}) - (p_{CW} - 2p_{2CW} + p_{2CCW} - 2p_{CCWCW})}{(p_{CCW} - 2p_{2CCW} + p_{2CW} - 2p_{CCWCW}) + (p_{CW} - 2p_{2CW} + p_{2CCW} - 2p_{CCWCW})}$$
$$= dir_0 \frac{1 - 3p_J}{1 - p_J(1 - 2\alpha + 2\alpha^2)}$$

As expected, and shown in Fig. 3d main text, the experimentally determined directionality decreases with increasing rotation frequency, since the likelihood of missing two jumps in the dominating direction, which are then recorded as one in the minor direction, is much higher than the reverse. In our experiment we find the time resolution to be about 1 ms, which is most likely limited by the feedback loop, needed for any constant current measurements.

The presented model holds true, as long as $(\alpha p_J)^3 \ll 1$ ($(\alpha p_J)^3 < 0.001$ in our experiments). If the frequency became larger, one would also have to consider the possibility of missing multiple rotation events.

Determination of the tunnel splitting ΔE_T and the tunneling frequency ν_{Th}

For the calculation of the energy splitting of the ground state $|\Psi_{00}>$ we have used the WKB approximation for a double barrier (3). For simplicity and comparability with the methyl tunnel rotation we have chosen a cosine line shape to represent the rotation potential $V(\phi) = \Delta E_B \cos^2(3\phi)$.

The ground state energy $E_{00} = \hbar\omega_{00}$ is obtained from the numerical solution of the Schrödinger equation of the rotational motion with $V(\phi)$ and the appropriate moment of inertia I. ϕ_a, ϕ_b and ϕ_c denote the angular position, where $V(\phi_i) = E_{00}$ as shown in Fig. S13.
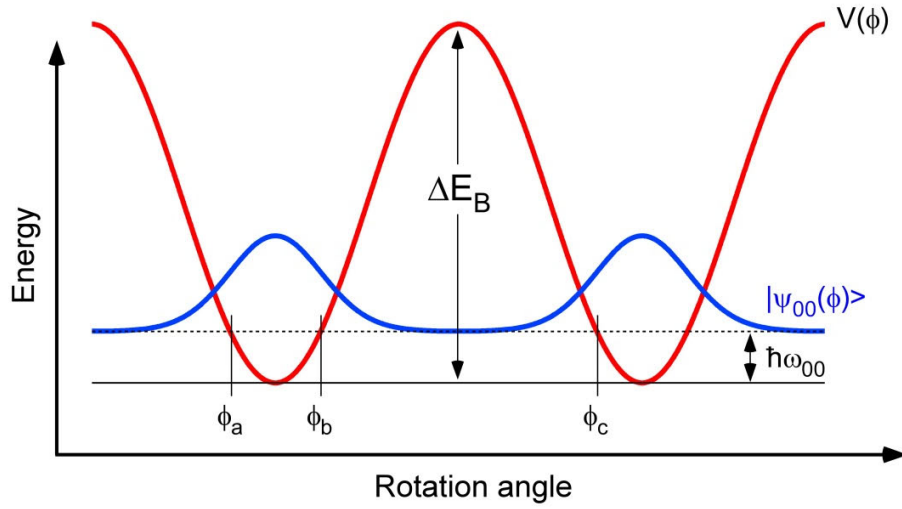

Fig. S13

Schematic representation of the double well tunneling in a $\cos(\phi)$ potential. With the ground state wave function shown in blue.

With the period of oscillation in the ground state given by:

$$\tau_0 = 2I \int_{\phi_a}^{\phi_b} \frac{d\phi}{\sqrt{2I(E_{00} - V(\phi))}}$$

We find for the tunnel splitting:

$$\Delta E_T = \frac{2\hbar}{\tau_0} exp\left[-\frac{1}{\hbar} \int_{\phi_b}^{\phi_c} \sqrt{2I(V(\phi) - E_{00})}d\phi \right]$$

With the tunnel frequency given by: $\quad \nu_T = \frac{\Delta E_T}{h}$

Table ST1 gives the tunneling splitting ΔE_T and tunneling frequency ν_{Th} of the acetylene for its different isotopes and compares them to other systems of tunneling transitions reported in literature.

System	I [kgm^2] m[kg]	Tunneling distance d_T [Å] or [rad]	ΔE_B [meV]	E_{00} [meV]	ΔE_T [meV]	ν_{Th} [MHz]
C$_2$H$_2$ / PdGa	I=5.62e-46	$\pi/3$ rad	25	3.58	0.0536	12.96
C$_2$HD / PdGa	I=6.20e-46	$\pi/3$ rad	25	3.42	0.02704	6.538
C$_2$D$_2$ / PdGa	I=6.87e-46	$\pi/3$ rad	25	3.25	0.0129	3.12
(CH$_3$)$_6$C$_6$ (3)	I=5.28e-47	$2\pi/3$ rad	86.5	10.9	0.0266	6.43
(CH$_3$)$_2$C$_2$N$_2$S (3)	I=5.28e-47	$2\pi/3$ rad	101	11.8	0.009	2.17
H/Cu(001) (4)	m=1.672e-27	2.55 Å	197	24.1	0.0355	8.59
D/Cu(001) (4)	m=3.344e-27	2.55 Å	194	17.1	5.22e-5	12.6e-3
H/Pt(111) (5)	m=1.672e-27	1.60 Å	190	36.7	20.8591	5.06e+3
Co/Cu(111) (6)	m=9.86e-26	1.55 Å	37	2.28	8.51e-10	0.2e-6

Table ST1

Comparison of the tunneling splitting and tunneling frequency (assuming a cosine double well in all cases) for different tunneling transitions
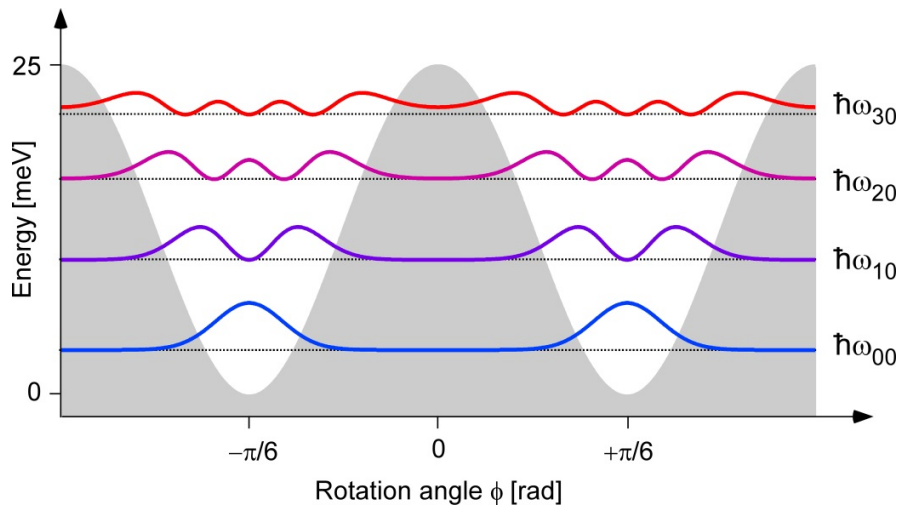

Fig. S14

Illustration of the 4 frustrated (bound) libration modes of the C$_2$H$_2$ with $\Delta E_B = 25\ meV$. The colored curves denote the probability density $\rho_n(\phi) = <\Psi_{n0}|\phi|\Psi_{n0}>$ of the states n=0,1,2,3.

System	I [kgm^2] m[kg]	Tunneling distance d_T [Å] or [rad]	ΔE_B [meV]	E_{n0} [meV]	ΔE_T [meV]	ν_{Th} [MHz]
C$_2$H$_2$ / PdGa	I=5.62e-46	π/3 rad	25	E$_{00}$=3.58	0.0536	12.96
C$_2$H$_2$ / PdGa	I=5.62e-46	π/3 rad	25	E$_{10}$=10.44	2.365	571.9
C$_2$H$_2$ / PdGa	I=5.62e-46	π/3 rad	25	E$_{20}$=16.54	43.70	10565
C$_2$H$_2$ / PdGa	I=5.62e-46	π/3 rad	25	E$_{30}$=21.44	327.92	79250

Table ST2

Tunneling splitting and tunneling frequencies for C$_2$H$_2$ and $\Delta E_B = 25\ meV$ for the $n = 0,1,2,3$ frustrated libration modes.

Experimental isotope dependence of the tunneling frequency

In order to have an indication that directed tunneling could be the explanation for the observed constant rotation frequency ν_T for $|V_G| \leq 30\,mV$ and $T < 15\,K$, ν_T was determined for C₂D₂, C₂DH and C₂H₂. As discussed in the section "Voltage and current dependence of the rotation frequency in the tunneling regime", the STM tip has a considerable impact on ν_T, therefore a meaningful comparison of ν_T for the different isotopes requires them to be measured with the same tip conditions. Accordingly, all three isotopes had to be accessible within at most 10 nm in the same STM frame (Fig. S15). Each color of Table ST3 corresponds to one measurement without any tip change in between. While the absolute frequencies vary significantly, the ratios of ν_T is shown to be independent of the polarity of the applied bias voltage and condition of the STM tip (Fig. S16).
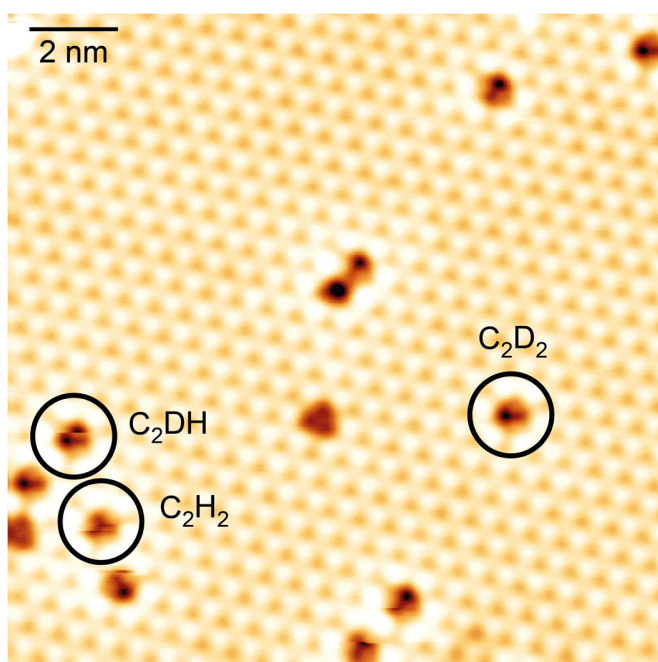

Fig. S15

STM image of C₂H₂, C₂DH and C₂D₂ adsorbed on Pd₃ ($T = 5\,K$, $V_G = 20\,mV$, $I_T = 20\,pA$). The data marked blue in ST3 has been recorded at these three molecules.
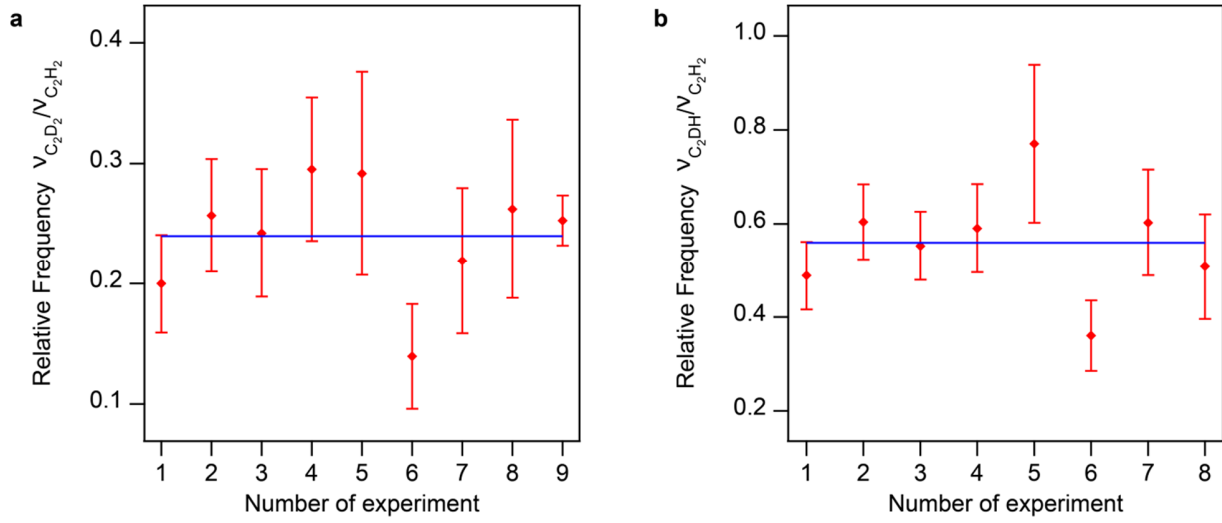
Fig. S16

Relative frequencies for each experiment (red markers) and their average (solid blue line) for both, **a** C_2D_2 and **b** C_2DH, compared to C_2H_2.

Bias	C_2D_2	C_2DH	C_2H_2	Time
-15 mV	0.054 ± 0.010 Hz	0.132 ± 0.016 Hz	0.270 ± 0.023 Hz	500 s
-5 mV	0.074 ± 0.012 Hz	0.174 ± 0.018 Hz	0.288 ± 0.024 Hz	500 s
+5 mV	0.078 ± 0.016 Hz Only 280 s	0.178 ± 0.019 Hz	0.322 ± 0.025 Hz	500 s
+15 mV	0.062 ± 0.011 Hz	0.124 ± 0.016 Hz	0.210 ± 0.020 Hz	500 s
-15 mV	0.028 ± 0.007 Hz	0.074 ± 0.012 Hz	0.096 ± 0.014 Hz	500 s
-5 mV	0.024 ± 0.007 Hz	0.062 ± 0.011 Hz	0.172 ± 0.019 Hz	500 s
+5 mV	0.032 ± 0.008 Hz	0.088 ± 0.013 Hz	0.146 ± 0.017 Hz	500 s
+15 mV	0.032 ± 0.008 Hz	0.062 ± 0.011 Hz	0.122 ± 0.016 Hz	500 s
+5 mV	0.108 ± 0.005 Hz	0.230 ± 0.010 Hz	NaN	5000 s (C_2D_2) 2500 s (C_2DH)
+ 10 mV	0.105 ± 0.006 Hz	0.259 ± 0.011 Hz	NaN	3000 s (C_2D_2) 2000s (C_2DH)
+5 mV	0.068 ± 0.005 Hz	NaN	0.269 ± 0.010 Hz	2500 s

Table ST3

Tunneling frequencies measured for all, C_2D_2, C_2DH and C_2H_2. The measurements taken without any change in the STM tip are marked with the same color in the most left column.

Movie SV1

The QuickTime-movie SV1.mov shows a sequence of 136 constant current STM images with 10 second time lapse between each frame. The movie shows two C_2H_2 motors, with the experimental settings written on top of the two panels. While the upper panel displays the raw STM data, the lower shows panel the corresponding interpolated (4 times the original pixel resolution) and contrast enhanced images. The contrast enhancement was achieved by subtracting each individual frame with the average of all 136 frames.

References

1. S. G. Tikhodeev, H. Ueba, How vibrationally assisted tunneling with STM affects the motions and reactions of single adsorbates. *Physical Review Letters* **102**, 246101 (2009).

2. Y. Kim, K. Motobayashi, T. Frederiksen, H. Ueba, M. Kawai, Action spectroscopy for single-molecule reactions – Experiments and theory. *Progress in Surface Science* **90**, 85–143 (2015).

3. M. Prager, A. Heidemann, Rotational tunneling and neutron spectroscopy: A compilation. *Chemical Reviews* **97**, 2933–2966 (1997).

4. L. J. Lauhon, W. Ho, Direct observation of the quantum tunneling of single hydrogen atoms with a scanning tunneling microscope. *Physical Review Letters* **85**, 4566–4569 (2000).

5. C. Z. Zheng, C. K. Yeung, M. M. T. Loy, X. Xiao, Quantum diffusion of H on Pt(111): Step effects. *Physical Review Letters* **97**, 166101 (2006).

6. J. A. Stroscio, R. J. Celotta, Controlling the dynamics of a single atom in lateral atom manipulation. *Science* **306**, 242–247 (2004).